Ceramics International 48 (2022) 31449–31460

Contents lists available at ScienceDirect

Ceramics International

journal homepage: www.elsevier.com/locate/ceramint

Functionalized silk promotes cell migration into calcium phosphate cements by providing macropores and cell adhesion motifs

Mona Widhe [a,1], Anna Diez-Escudero [b,1], Yuling Liu [c], Nathalie Ringström [a], Maria-Pau Ginebra [d,e], Cecilia Persson [c], My Hedhammar [a], Gemma Mestres [c,f,*]

[a] Division of Protein Technology, School of Chemistry, Biotechnology and Health (CBH), KTH Royal Institute of Technology, SE-106 91, Stockholm, Sweden
[b] Ortholab, Department of Surgical Sciences, Orthopaedics, Uppsala University, 751 85, Uppsala, Sweden
[c] Division of Biomedical Engineering, Department of Materials Science and Engineering, Uppsala University, 751 22, Uppsala, Sweden
[d] Biomaterials, Biomechanics and Tissue Engineering Group, Department of Materials Science and Engineering, Research Centre for Biomedical Engineering (CREB), Universitat Politècnica de Catalunya (UPC), 08019, Barcelona, Spain
[e] Institute for Bioengineering of Catalonia (IBEC), Barcelona Institute of Science and Technology, Baldiri Reixac 10- 12, 08028, Barcelona, Spain
[f] Science for Life Laboratory, Uppsala University, 751 22, Uppsala, Sweden

ARTICLE INFO

Keywords:
Bone regeneration
Hydroxyapatite
RGD motifs
Silk

ABSTRACT

Calcium phosphate cements (CPCs) are attractive synthetic bone grafts as they possess osteoconductive and osteoinductive properties. Their biomimetic synthesis grants them an intrinsic nano- and microporosity that resembles natural bone and is paramount for biological processes such as protein adhesion, which can later enhance cell adhesion. However, a main limitation of CPCs is the lack of macroporosity, which is crucial to allow cell colonization throughout the scaffold. Moreover, CPCs lack specific motifs to guide cell interactions through their membrane proteins. In this study, we explore a strategy targeting simultaneously both macroporosity and cell binding motifs within CPCs by the use of recombinant silk. A silk protein functionalized with the cell binding motif RGD serves as foaming template of CPCs to achieve biomimetic hydroxyapatite (HA) scaffolds with multiscale porosity. The synergies of RGD-motifs in the silk macroporous template and the biomimetic features of HA are explored for their potential to enhance mesenchymal stem cell adhesion, proliferation, migration and differentiation. Macroporous Silk-HA scaffolds improve initial cell adhesion compared to a macroporous HA in the absence of silk, and importantly, the presence of silk greatly enhances cell migration into the scaffold. Additionally, cell proliferation and osteogenic differentiation are achieved in the scaffolds.

1. Introduction

Bone tissue engineering comprises the development and application of synthetic scaffolds that can promote bone regeneration. Autografts are today the gold standard treatment for bone regeneration, especially in critical size defects, although autografts have drawbacks such as limited availability, entailing invasive clinical procedures and comorbidity to patients. Synthetic bone grafts are a consolidated alternative to treat bone defects, however, producing an ideal bone graft is not trivial. Depending on their application, bone grafts are required to be biocompatible and support bone growth. Furthermore, in tissue regenerative approaches, they should enhance and induce cell growth and differentiation, serving as temporary templates for new bone growth [1,2]. One of the main challenges in bone regeneration is to achieve a good balance between biomaterial resorption and bone formation [3–5], which have to be accompanied with angiogenesis to deliver oxygen and nutrients to the colonizing cells [6]. Porosity can be pointed out as one of the most important parameters to achieve this balance, where total porosity, pore size distribution and pore interconnectivity play important roles [7]. In addition, it is known that a hierarchical porosity is crucial for the interaction with the biological environment. In particular, pores within the nano- and micrometer range enhance the adsorption and entrapment of proteins, which subsequently provide biological cues to the cells [8,9]. To facilitate cellular colonization followed by bone formation, it has been estimated that scaffolds should have interconnected porosity and a pore size between 100 and 400 μm [8–11].

* Corresponding author. Division of Biomedical Engineering, Department of Materials Science and Engineering, Uppsala University, 751 22, Uppsala, Sweden.
E-mail address: gemma.mestres@angstrom.uu.se (G. Mestres).
[1] Contributed equally to the article.

https://doi.org/10.1016/j.ceramint.2022.07.056
Received 21 May 2022; Received in revised form 28 June 2022; Accepted 6 July 2022
Available online 14 July 2022

Finally, to achieve a successful viable scaffold for tissue engineering, cells should be evenly distributed throughout the entire volume of the scaffold [12].

The scientific community has developed a huge variety of biomaterials for bone regeneration. Within those, calcium deficient hydroxyapatite (abbreviated as HA), produced from calcium phosphate cements (CPCs), has attracted special attention because it closely resembles the mineral phase of the bone [13,14] and it has excellent biocompatibility and osteoconductive properties, as well as potential osteoinductive properties under certain conformations [15]. In addition, HA has an intrinsic high total porosity (~ 30–55%) due to voids left between crystals and the spaces separating the crystals agglomerates [16]. Since HA's inherent porosity is within the micrometric size, the macroporosity needed for cell colonization has to be extrinsically introduced during processing of the materials. The methodologies more commonly used for this purpose are casting processes (using a mold or impregnating a sacrificial macroporous template) [17,18], usage of sacrificial crystals or microspheres [12,19–21], foaming processes using surfactant agents (to entrap air within a matrix) [22–25] or a combination thereof [26]. These methodologies are simple, quick and do not require specialized equipment. However, they provide irregular pores and potentially insufficient interconnectivity [3]. Higher control over the spatial distribution of the pores can be achieved with additive manufacturing after optimizing the resolution to produce adequate pores [3,27–30].

The use of silk-based materials in combination with hydroxyapatite has been exploited using silk from Bombyx mori as a template to incorporate macroporosity [31]. However, in those studies the silk was burnt during sintering, and therefore the potential positive effects of silk for cell interactions were not exploited [32]. An emerging alternative is the use of recombinantly produced silk as biomaterial for biomedical applications [33] since it has been shown to be cytocompatible [34–37] and biocompatible [38]. Moreover, silk proteins have the inherent ability to self-assemble under physiological-like conditions [37,39] and can be transformed into several different macroscopic structures, *e.g.* film, fibers and foam [34]. In particular, FN-silk, a partial spider silk protein functionalized with the cell binding motif RGD presented on a looped structure derived from the human ECM protein fibronectin, has been shown to markedly increase cellular attachment, spreading, proliferation and migration compared to silk without cell binding motifs [35,36]. Previous studies have also explored the incorporation of RGD-motifs into CPCs, evidencing an improvement in cell behavior in terms of cell spreading, proliferation and upregulation of osteogenic related genes. Usually, the incorporation of RGD is achieved through prior functionalization to covalently link the RGD to a template such as chitosan that is later used as a liquid carrier in the CPC formulation [40–42]. In other approaches, RGD has been incorporated as a powder directly onto the CPC or as impregnating solution, demonstrating enhanced mesenchymal stem cells differentiation [43] and bone formation *in vivo* [44], although lacking macroporosity. Despite the previous studies on the incorporation of cell binding motifs into CPCs, the combination of FN-silk containing RGD as both macroporous template and biofunctionalization molecule into CDHA-based CPCs has not yet been reported.

The aim of this work was to evaluate the capacity of FN-silk to introduce macroporosity to HA and determine the influence of the FN-silk on cell response. Macroporous silk-HA scaffolds (Macro Silk-HA) were fabricated and compared to macroporous HA obtained with the synthetic non-ionic soluble surfactant polysorbate 80 (Macro HA). For both scaffold types, the resulting total porosity was assessed both in terms of the foaming agent concentration and the addition of an accelerant (sodium hydrogen phosphate). As control, a dense HA was used. MSCs were cultured on the scaffolds, and initial cell adhesion was analyzed, followed by evaluation of cell proliferation, differentiation and migration along the 21 days of culture.

2. Experimental section

2.1. Preparation of alpha-TCP (α-TCP)

Alpha-tricalcium phosphate (α-TCP, α-$Ca_3(PO_4)_2$) was produced by mixing calcium hydrogen phosphate ($CaHPO_4$, Sigma C7263, ref. n. MKCC6144) and calcium carbonate ($CaCO_3$, ACROS Organics, ref. n. 423515000) at a 2:1 M ratio. The mixture was heated on a zirconia setter plate for 15 h at 1400 °C in a furnace (Entech MF 4/16) followed by quenching in air, as previously reported [7].

The α-TCP obtained (100 g) was milled for 15 min at 300 rpm in a planetary ball mill (PM400, Retsch, Germany) using a zirconia bowl and 100 zirconia balls (Ø = 5 mm). After milling, α-TCP was supplemented with 2 wt % hydroxyapatite (HA, Merck, Darmstadt, Germany) to act as a seed. In addition, 2.5 wt % $Na_2HPO_4{\cdot}2H_2O$ (NaP, Sigma-Aldrich, ref. n. 71643) was added to the powder phase (solid phase, SP), and ended up in the solid phase of calcium phosphate cements (CPCs). NaP acts as a common ion accelerating the precipitation and formation of calcium deficient hydroxyapatite (CDHA), and was added to the powder phase of the cement (instead of the liquid phase) to avoid influencing the foamability of the liquid phase.

2.2. Silk protein

The recombinant FN-silk protein, a partial dragline silk major ampullate Spidroin 1 (MaSp1) functionalized with an RGD motif from human fibronectin [36], was kindly provided by Spiber Technologies AB. The protein is produced in *E. coli*, purified using chromatographic methods [39,45] to lipopolysaccharide (LPS) levels below 150 EU/mL, and subjected to sterile filtration before storage at −20 °C.

2.3. Preparation of calcium phosphate foams (macroporous) and calcium phosphate cements (dense)

Two types of macroporous HA, one containing silk protein (Macro Silk-HA) and the other one prepared with a soluble non-ionic surfactant (Macro HA), were made by mixing α-TCP powder with a liquid phase containing the foaming agent. In addition, an unfoamed CPC was prepared mixing α-TCP powder with plain MilliQ water as liquid phase (Dense HA). A liquid-to-powder ratio of 0.65 mL/g was used for the three materials developed.

The liquid phase (LP) of the macroporous HAs contained either 2 mg/mL FN-silk in phosphate buffered saline (PBS, Sigma Aldrich) or 0.05–0.75 w/v % polysorbate 80 (PS80, Tween 80TM, Sigma-Aldrich, ref. n. P1754) in MilliQ water. Three mL of the liquid phase were placed in a 30 mL beaker and foamed with a handheld milk frother (IKEA, ref. n. 503.011.66). For the FN-silk solution, the liquid phase was first whipped for 5–7 s to create a foam, and then the powder was added in three steps, each followed by 3–5 s of further whipping. The silk protein concentration and the foaming procedure were previously optimized for the Macro Silk-HA (Fig. A2). For the macroporous samples prepared with PS, the solid phase was added to the liquid phase and the mixture was whipped for 30 s in a single step. The final compositions selected for the solid and liquid phase as well as the mixing method used are summarized in Table 1.

The cement pastes were carefully transferred into silicon molds (Ø = 12 mm, h = 1 mm) and left for setting in saturated humidity at 37 °C overnight (i.e. 16 h). Afterwards, the set samples were immersed in PBS for 10 days for full reaction into calcium deficient hydroxyapatite (HA). The procedure to foam the liquid phase, prepare and set the cements is schematically depicted in Fig. 1. The set HA samples were named according to their porosity and presence of silk. Therefore, Macro Silk-HA refers to the cement foamed with silk, Macro HA refers to the cement foamed with PS80, and Dense HA refers to the cement manually mixed.

Table 1
Sample composition and mixing method. The liquid-to-powder ratio was 0.65 mL/g for all samples (α-TCP: α-tricalcium phosphate; NaP: Na_2HPO_4 added in the solid phase; PS80: polysorbate 80 added in the liquid phase, PBS: phosphate buffer solution).

Sample	Solid phase	Liquid phase	Method to mix and foam the cement paste
Macro Silk-HA	α-TCP+ 2 wt% HA+ 2.5 wt% NaP[a]	2 mg/ml silk in PBS	Liquid phase foamed first (5–7 s) and solid phase added in 3 steps (mixed/foamed for 3–5 s in each step)
Macro HA		0.1 wt/v% PS in MilliQ water (PS80)[a]	Solid phase and liquid phase mixed/foamed simultaneously for 30 s (1 step)
Dense HA		MilliQ water	Manually mixed with a spatula

[a] Different concentrations of NaP and PS80 were tested in initial optimization experiments.

2.4. Physico-chemical characterizations

The crystalline phases present in the HA scaffolds were analyzed by X-ray diffraction (XRD) using a D8 Twin-Twin diffractometer equipped with a Bragg–Brentano geometry and CuKα radiation. The analysis was performed between 10 and 50°, with a time per step of 96 s, a step size of 0.014°, voltage 40 kV and intensity 40 mA when rotating the sample at 80 rpm. The samples were compared to standards of α-TCP and HA (JCPDS 04-010-4348 and 01-074-0565, respectively). Profex (http://profex.doebelin.org) [46] in combination with BGMN (http://www.bgmn.de) [47,48] were used to quantitatively analyze the powder XRD data by Rietveld refinement. For this purpose, structural models for α-TCP (ICSD No. 923) and HA (ICSD No. 151414) from the Inorganic Crystal Structure Database (ICSD) were used [49]. Good structure refinements were achieved by varying the scale factor, background coefficients and unit-cell axes (a = b and c).

To determine the total porosity of the samples, micro-computed tomography μCT (Skyscan 1072, Bruker, Kontich, Belgium) was performed using triplicates. Specimens were scanned using a source voltage of 100 kV, a current of 100 μA, a 5 mm aluminum + cupper filter, and an isotropic pixel size of 6.79 μm. Three-D reconstructions and calculations were performed using software package NRecon and CTAN (SkyScan, Bruker, Kontich, Belgium), respectively. The pore entrance size distribution was measured by mercury intrusion porosimetry (MIP, Autopore IV 9500, Micromeritics, USA) using 7 samples in the holder in a single measurement. The mercury intrusion-extrusion curves were recorded from 0.5 to 30,000 psia.

The morphological features of each sample were analyzed by scanning electron microscopy (SEM). Prior to visualization, a thin layer of gold/palladium of approximately 5 nm was sputtered on the sample surface. For the optimization part (evaluation of the effect of both NaP and PS80 concentrations), a tabletop SEM (Hitachi TM4000) was used, whereas a Field Emission SEM (FE-SEM, Merlin Zeiss, Germany) was employed to analyze the final specimens.

2.5. Biological characterization, cell culture

Bone marrow derived mouse (C57BL/6) mesenchymal stem cells (mMSC, Gibco, ref. n. S1502-100) were expanded in Dulbecco's Modified Eagle's Medium/Nutrient Mixture F-12 Ham (DMEM F-12 Ham) (Gibco, ref. n. 11330-057) with 10% mesenchymal stem cell certified FBS (Gibco, ref. n. 12662-029), 1% penicillin-streptomycin and 15 mM HEPES buffer. Medium was changed every second day.

Prior to cell seeding, the scaffolds were sterilized in 70% ethanol for 3 h and then extensively washed 3 × 15 min in excess of PBS at room temperature (RT) [50]. Afterwards, each scaffold was pre-incubated in 3 mL of complete cell culture medium for 3 days at 37 °C with 5% CO_2 and 95% humidity to avoid ionic changes in the media due to the CPC reactive nature prior to seeding.

mMSCs at passage 9 were harvested at 70% confluency and seeded in five replicates onto the scaffolds at 40,000 cells/cm^2 in 1 mL culture medium. Cells were allowed to adhere for 3 h in the incubator, or left in culture for 1, 4, 7, 14 or 21 days. The first week the cells were in culture medium, and the last two weeks in differentiation medium, which was cell culture medium supplemented with 50 μg/mL L-sodium ascorbate (Sigma A-7631), 10 mM β-glycerophosphate (Sigma G-9422) and 50 μg/mL dexamethasone (Sigma D-4902) [51]. Medium was changed every day during the first week, and afterwards every second day.

Cellular adhesion, proliferation, differentiation and infiltration degree were evaluated at culture day 1, 4, 7, 14 and 21.

2.6. Biological characterization, cell enumeration

Lactate dehydrogenase (LDH) assay was used to evaluate cell growth. This assay is a mean of indirectly measuring the number of viable cells present in a culture via total cytoplasmic LDH. Prior to performing LDH analysis, scaffolds were washed three times with PBS to remove any dead cells or cell debris, and the cells remaining on or inside the scaffold were lysed according to instructions provided in the LDH kit (TOX7, Sigma-Aldrich). To ensure proper cell detachment from the scaffold, the

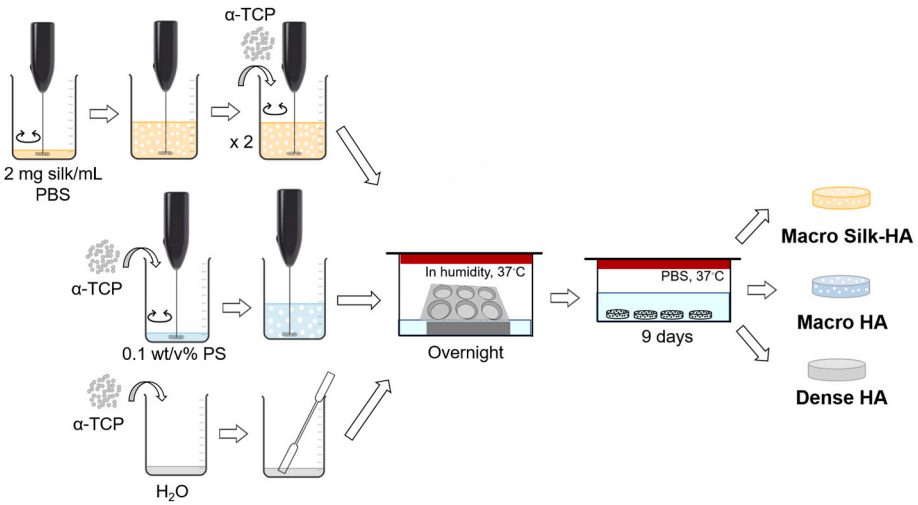

Fig. 1. Schematic showing the preparation steps for Macro Silk-HA, Macro HA and Dense HA (PBS: phosphate buffer solution; α -TCP: α-$Ca_3(PO_4)_2$; PS: polysorbate 80, H_2O: MilliQ distilled water).

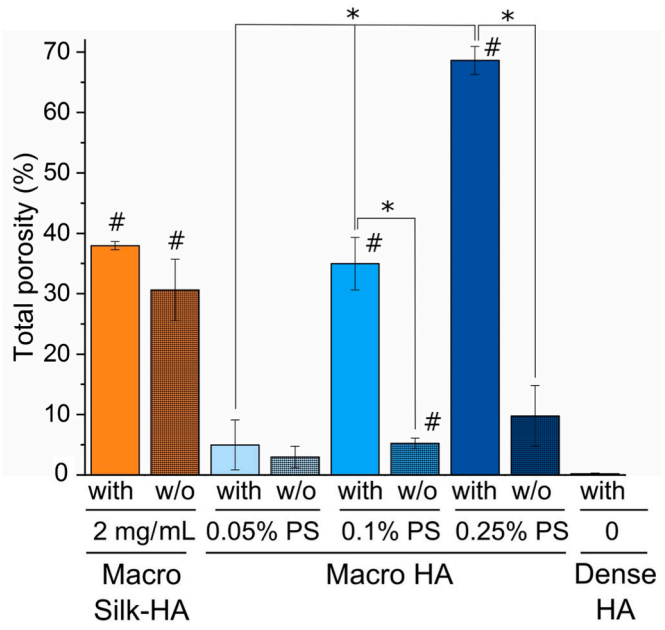

Fig. 2. Porosity measured by μ-CT of Macro Silk-HA (2 mg/mL), Macrco HA (0.05, 0.10 and 0.25 w/v% PS80) and dense HA. The presence (w) or absence (wo) of 2.5 wt% NaP is indicated. * indicates statistically significant differences between groups while # displays statistical differences compared to Dense HA.

lysates were harshly pipetted onto the scaffolds before centrifugation at 500×*g* for 5 min.

After cell lysis, the LDH assay was performed as per manufacturer's instructions. Briefly, 40 μL of the cell lysates were added in triplicates to a 96-well plate (Greiner #655161). Next, 80 μL of an assay mixture containing equal parts of substrate, cofactor and dye reagents from the kit was then added to each well. The plate was allowed to incubate in darkness at RT for 20 min, and then the reaction was stopped by adding 10 v/v % 1 N HCl. OD490 was measured in a CLARIOStar (BMG Labtech, Germany) with OD690 used as reference wavelength. The resulting OD values were transformed to cell number using a 1:5 dilution series of 7 standard points (range 64 cells -10^6 cells) to construct a standard curve through four-parameter fit (GraphPad Prism 8).

2.7. Biological characterization, osteogenic cell differentiation

Alkaline phosphatase (ALP) activity was analyzed to evaluate the osteogenic differentiation of mMSCs cultured on the scaffolds. To assess the ALP activity, the substrate p-nitrophenyl phosphate (pNPP, Sigma-Aldrich 71768) at 4 mg/mL was mixed with 1.5 M alkaline buffer (Sigma-Aldrich A9226) and added to the cell lysates (same ones as used for LDH assay) in triplicates. OD410 was measured once every minute for 30 min using a CLARIOStar reader. OD410 values were converted to product concentration using the adsorption coefficient of p-nitrophenol. Thereafter, the ALP activity level was calculated by the slope of the concentration plot, and finally the activity level was normalized by the total number of cells (Fig. A5).

2.8. Biological characterization, cell attachment and morphology by fluorescence microscopy analysis

Single scaffolds were selected for imaging after 3 h, 7, 14 and 21 days of culture. Prior to fixation, the scaffolds were washed twice with pre-warmed PBS to remove any dead cells or cell debris. Cells were fixed with 4% paraformaldehyde (PFA) for 15 min at RT, and the scaffolds were stored in PBS at 4 °C.

The fixed scaffolds were permeabilized in 0.2 w/v% Triton-100 for 3–5 min and blocked in 1 w/v% bovine serum albumin (BSA) in PBS for 20 min. Afterwards, the scaffolds were stained for F-actin using Phalloidin-AlexaFluor488 or AlexaFluor546 (Invitrogen, ref. n. A11034 and A11003) diluted in 1:40 PBS with 1 w/v % BSA, for 60 min in darkness. Finally, DAPI 1:1000 in PBS was used for nuclear staining and the stained scaffolds were stored in PBS at 4 °C.

Imaging was performed using an inverted fluorescence microscope (Nikon Eclipse Ti, Nikon, Netherlands). The filters "UV", "GFP" and "Texas Red" (Nikon) were used to capture the fluorescence by DAPI, AlexaFluor488 and AlexaFluor546, respectively. Micrographs were captured using a Zyla 5.5 sCMOS camera (Andor, Oxford Instruments, UK) and the NIS-elements BR software (Nikon).

2.9. Biological characterization, infiltration and migration measurements

After fluorescence imaging, the scaffolds were soaked in 20% sucrose overnight to prevent cryodamage, and then embedded in an optimal cutting temperature compound (OCT, Cellpath™, KMA-0100-00A, UK) at −20 °C. Using a cryostat (Leica CM3050S), 25 μm thick cross sections were collected on SuperFrost Plus microscope glasses (Thermo Scientific, ref. n. J1800AMNZ), and stored dark at RT. The sectioning was performed along the length of the cross section to avoid smearing of cells from the scaffold top surface towards the inner parts. Imaging was performed using an inverted fluorescence microscope as described above.

Cellular infiltration and migration into the scaffolds were assessed by measuring the distance from the scaffold surface (seeded side) to the position of individual cells, using the manual measurement tool in NIS elements (Nikon). For each scaffold, three sections were evaluated with at least 10 points of measurements. The measurement points were set to be evenly spread along the length of the section and, at each point, the cell that had migrated the most was selected for measurement, altogether yielding a measure of the infiltration degree. To be able to estimate the total migrated distance of the cells during the 3 weeks culture period, the distance to the scaffold surface at 3 h was subtracted from the distance at day 21, and referred to as migration distance.

2.10. Biological characterization, cell morphology by SEM

The previously fixed and stained samples were further imaged by SEM, using scaffolds cultured for 3 h, 7 and 21 days. The scaffolds with cells were dehydrated in increasing ethanol series (10, 30, 50, 70, 90% and absolute ethanol) for 15 min each, and finally allowed to dry inside a fume hood. Dehydrated samples were sputtered with a gold-palladium layer of approximately 5–7 nm to impart conductivity, and imaged by SEM (FE-SEM, Merlin Zeiss, Germany), at 3 kV acceleration voltage.

2.11. Statistical analysis

For all experiments, three independent experiments using triplicates were performed. The results are presented as mean ± standard deviation of three independent experiments. Statistical analysis was performed using Minitab version 18. The data was evaluated by one-way analysis of variance (ANOVA), two-sided, at a significance level of $\alpha = 0.05$. Post-hoc Tukey test was performed to investigate differences between groups. A Levene's test was used to assess homogeneity of variances between groups. When significant, Welch's ANOVA, with post-hoc Games-Howell test was used to assess differences between groups. P-values < 0.05 were considered statistically significant.

3. Results

First, the initial reagents were evaluated. The alpha-tricalcium phosphate (α-TCP) powder was characterized, confirming composition and particle size (Fig. A1), and the effect of the two foaming agents (silk and polysorbate) on foamability and foam stability was investigated (Fig. A2). Afterwards, the composition of the macroporous cements was

optimized to yield two types of macroporous HA (with and without silk) with similar levels of total porosity. When these were established, mMSCs were cultured on the optimized scaffolds to evaluate their proliferation, differentiation and migration.

3.1. Optimization of macroporous calcium phosphate cements

An initial study with three concentrations of silk protein (1.5, 2 and 3 mg/mL) indicated that while the total porosity slightly increased with a higher concentration of silk, the results were not significantly different (Fig. A3a). Therefore, the intermediate concentration of 2 mg/mL was selected to reduce the amount of recombinant protein needed by a third. Thereafter, the effect of foaming time and method to flatten the samples in the mold was evaluated. In order to maximize the total porosity, a procedure with a short foaming time followed by tapping the mold containing the samples (without use of a spatula) was chosen (Fig. A3b). This procedure (with intermediate silk concentration, short foaming and tapping) was used for the rest of the study.

The possible effect of the surfactant polysorbate (PS80) in combination with the accelerant $Na_2HPO_4{\cdot}2H_2O$ (NaP) on the porosity of the samples was evaluated by microcomputed tomography (μCT). Without NaP, the porosity only increased slightly when augmenting the PS80, reaching a total porosity of 9.8 ± 5.0% with a PS80 of 0.25 w/v%. However, with presence of NaP a statistically significant increase in total porosity was observed by augmenting the concentration from 0.05 to 0.10% ($p = 0.0005$) and from 0.10 to 0.25% ($p = 0.0005$), reaching a total porosity of 68.6 ± 2.3% for a PS80 of 0.25 w/v%. In contrast, the presence of NaP only slightly increased the already rather high (30.6 ± 5.0%) total porosity of Macro Silk-HA samples, resulting in a total porosity of 38.0 ± 0.7% (Fig. 2). Thus, further physico-chemical characterization and biological studies were performed with macroporous HA containing PS80 of 0.1 w/v% together with NaP, since that yielded macroporosity levels similar to those of Macro Silk-HA with NaP (35.0 ± 3.6% for Macro HA, and 38.0 ± 0.7% for Macro Silk-HA). Both macroporous samples containing NaP had a significant higher total porosity than Dense HA ($p < 0.005$ for both Macro Silk-HA and Macro HA).

From now onwards, the physico-chemical and biological properties were investigated on optimized compositions consisting of: Macro Silk-HA prepared with 2 mg/mL FN-silk, Macro HA prepared with 0.1 w/v% PS80, and Dense HA, all three compositions containing 2.5 wt% NaP. The effects of NaP addition when using PS80 (0.1 w/v%) or silk (2 mg/mL) were then analyzed by scanning electron microscopy (SEM), depicting an increase on the porosity for both Macro HA and Macro Silk-HA, this being most evident for the former one (Fig. 3). The presence of NaP substantially increased superficial pore sizes (Fig. 3a, c), whereas the effects were less obvious when looking at cross-sections (Fig. 3f, h). Dense HA showed a compact structure both at the surface and in the bulk (Fig. 3e, j).

3.2. Physico-chemical characterization

Crystalline phase analysis performed by X-ray diffraction (XRD) and quantified by Rietveld refinement revealed that the α-TCP had almost completely transformed into CDHA in the three sample types, with a range between 93 and 97% (Fig. A4 and Table A.2). The addition of PS80 and silk seemed to slightly enhance the CDHA transformation, most pronounced in the Macro-silk-HA.

The interconnected porosity of the three optimized materials was analyzed by mercury intrusion porosimetry (MIP), which determines the pore entrance size diameter (PESD). The types of pores observed were grouped in three ranges: i) intercrystals' porosity, pores caused by the distance between crystals (0.006–0.6 μm); ii) interaggregates' porosity, pores related to the distance between agglomerates of crystals (0.6–4.1 μm); and iii) extrinsic porosity, introduced by foaming (4.1–360 μm). The MIP results are shown in Fig. 4a as a distribution of pores, which were further quantified according to pore ranges in Fig. 4b. The wide PESD band visualized within the submicrometer range accounted for ~15% for both Silk Macro-HA and Macro HA, and almost 20% for Dense HA. Within the 0.6–4.1 μm range, a prominent peak was found for all materials, where Dense HA had the highest amount of pores (27.6%), followed by Macro HA (20.7%) and Macro Silk-HA (14.9%). No more significant peaks were detected for Dense HA and its total porosity at PESD higher than 4.1 μm accounted for only a 5.6%. Both macroporous HAs displayed a peak of extrinsic porosity between 4.5 and 12 μm, Macro Silk-HA (5.4%) having a slightly higher quantity of these pore sizes compared to Macro HA (4.0%). Still within the range of extrinsic porosity, Macro HA showed a large peak between 12 and 115 μm (16.0%) and a smaller one between 141 and 303 μm (3.1%). In the case of Macro Silk-HA, two small peaks were detected within 45 and 74 μm (0.9%) and within 80 and 140 μm (1.8%). In total, the extrinsic porosity measured by MIP accounted for 11.8% in Macro Silk-HA and 24.3% in Macro HA (Figure 4).

The structure of the porosity was further analyzed by SEM. The surface images showed that Macro Silk-HA (Fig. 5a) had a larger quantity of pores, which were more heterogeneous in size and generally smaller than in Macro HA (Fig. 5b). Similarly, on the cross-section, the Macro Silk-HA (Fig. 5d) showed smaller pores and the pore interconnections were also smaller than for Macro HA (Fig. 5e). Dense HA did not display any macropores, neither on the surface nor on the cross-section (Fig. 5c and f). Looking at the cross-section at a higher magnification, a plate-like structure of small plates was observed for Macro HA

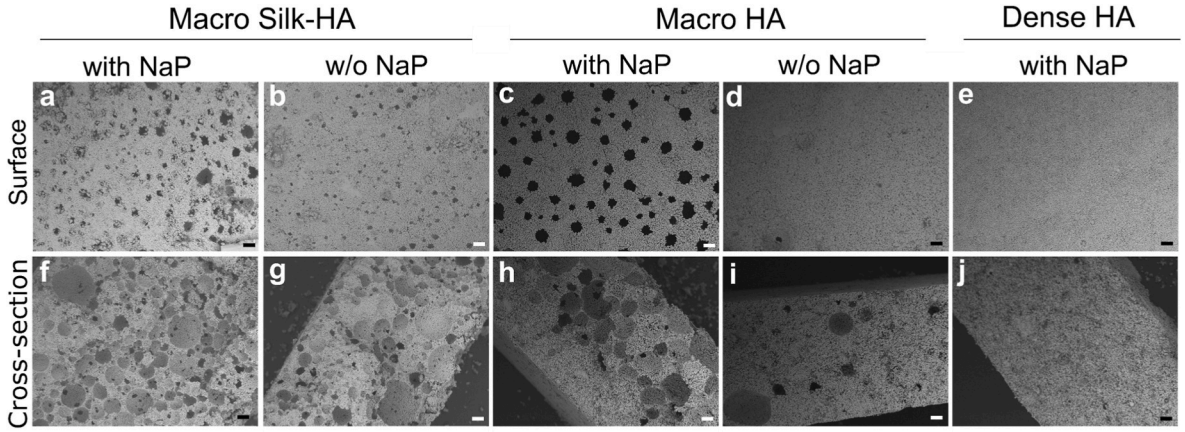

Fig. 3. SEM images of the surface and cross-section of Macro Silk-HA (2 mg/mL FN-silk) and Macro HA (0.1 w/v% PS80), which were prepared in the presence (with) and absence (w/o) of 2.5 wt% NaP, and Dense HA (with 2.5 wt% NaP). Micrographs were taken with a SEM equipment Hitachi TM4000. Scale bar 100 μm.

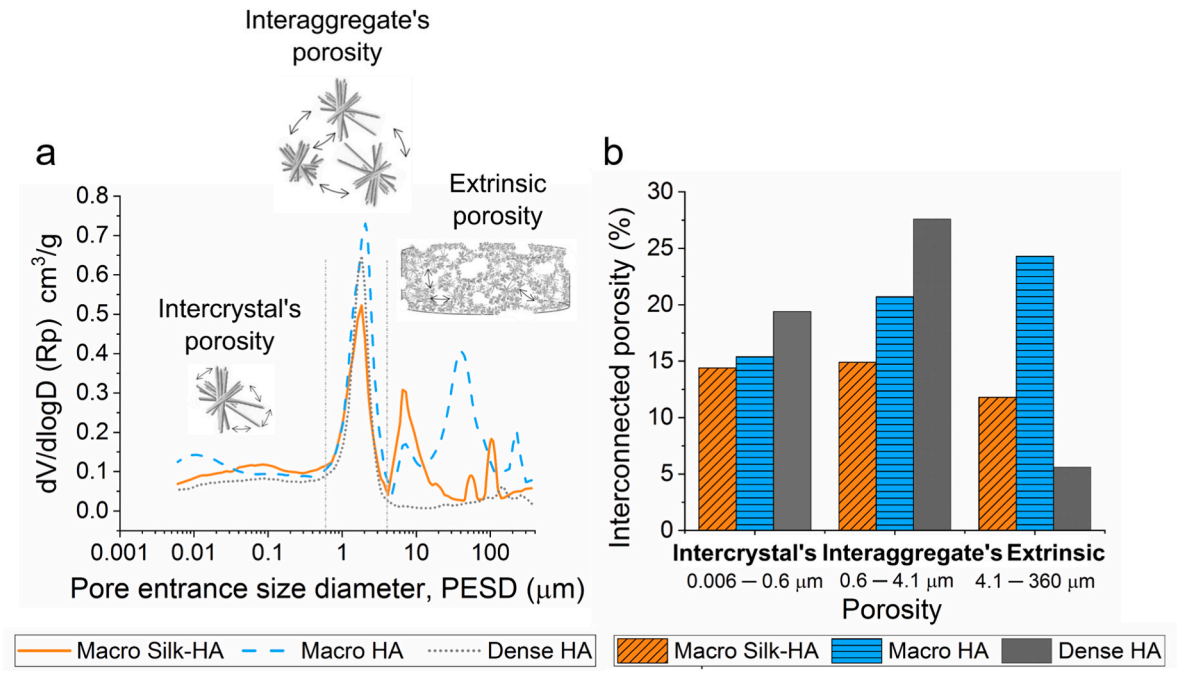

Fig. 4. Pore entrance size analyzed by MIP displayed as MIP pore entry size distribution (PESD) (a) and percentage of interconnected porosity within the intercrystal's, interaggregates' and extrinsic porosity range (b).

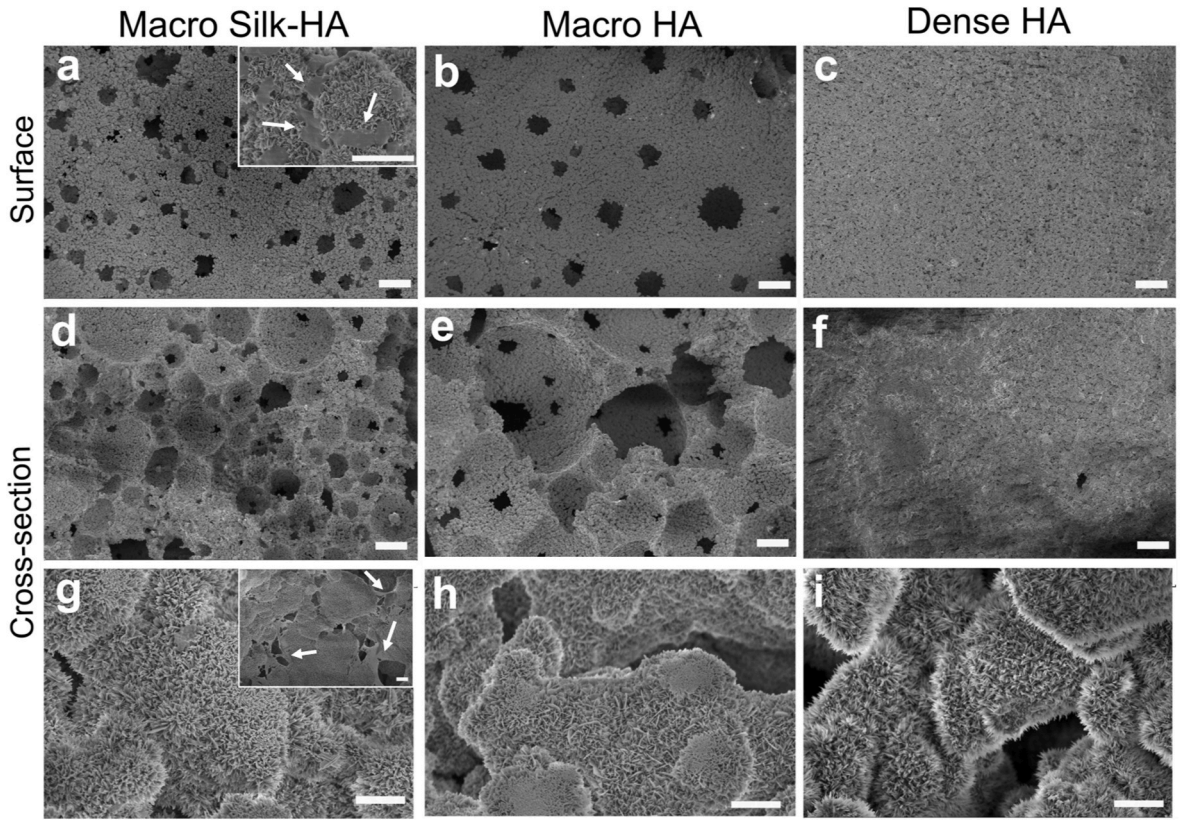

Fig. 5. Morphological characterization of the optimized samples by SEM. Micrographies were taken with a Field Emission SEM both at the surface and cross-sections of Macro Silk-HA (a, d, g), Macro HA (b, e, h) and Dense HA (c, f, i). The white arrows point to the silk. Scale bars (a–f): 100 μm and (g-i and two insert images in a and g): 2 μm.

and Macro Silk-HA (Fig. 5g and h), whereas Dense HA displayed a needle like structure (Fig. 5i). At high magnifications, the silk was clearly observed, both at the surface and at cross-sections of the material (Fig. 5a and g insets, white arrows).

3.3. Biological characterization

The biocompatibility and osteoconductive properties of the HA-scaffolds were evaluated by the analysis of attachment, proliferation, differentiation and migration of bone marrow derived mouse mesenchymal stem cells (mMSCs) initially seeded on the scaffold surface.

3.3.1. Initial cell attachment and morphology

Inverted fluorescence microscopy analysis showed that, already after 3 h, a high number of mMSCs had attached and started to spread on the top surface of the scaffolds (Fig. 6a). At this initial stage, the cell area gives an indication of how far the attachment process has proceeded: the larger the cell, the better the attachment. Cells seeded on Macro HA (both with and without silk) appeared larger than cells on the Dense-HA at this early time point (Fig. 6a). However, cells quickly increased in number and achieved a more elongated shape during culture on all scaffold types (Fig. A6).

3.3.2. Cell growth

A lactate dehydrogenase (LDH) activity assay was used to quantify the number of cells populating the scaffolds at five different time points during the 3 weeks culture period, enabling comparison of growth profiles for cells in the different scaffold types. The mMSCs showed a clear expansion phase during the first week of culture on all three scaffold types (Fig. 6b), which during the second and third week flattened out as the cells became more confluent. The cells initially grew faster on the Macro HA, but the advantage over the Macro Silk-HA decreased over time. From day 14, equal number of cells were detected in the two porous scaffold types. This growth pattern was supported by analysis of top view stainings of the scaffolds taken at different time points during the culture (Fig. A6). From 7 days of cell culture, the cell layer observed on Macro Silk-HA had most prominent actin filaments, indicating good attachment. Three weeks after seeding, an almost completely confluent mat of cells was observed on the surface of all scaffold types (Fig. A6 and A.7).

3.3.3. Osteogenic differentiation

Different markers for osteogenic activity can be used to verify that cells mature and differentiate into bone. Alkaline phosphatase (ALP) is expressed early in the differentiation process of osteoblasts [52], and high levels have been identified as a robust *in vitro* marker for bone formation of bone marrow stromal cells [53]. Therefore, an ALP activity assay was used to evaluate the potential of the HA materials to support osteogenic differentiation of the mMSCs.

During the first week of culture, when the cells were cultured in regular growth medium, very low activity of ALP was detected in cell lysates from the three scaffold types. At 7 days after seeding, i.e. upon addition of osteogenic factors to the medium, the ALP-activity had

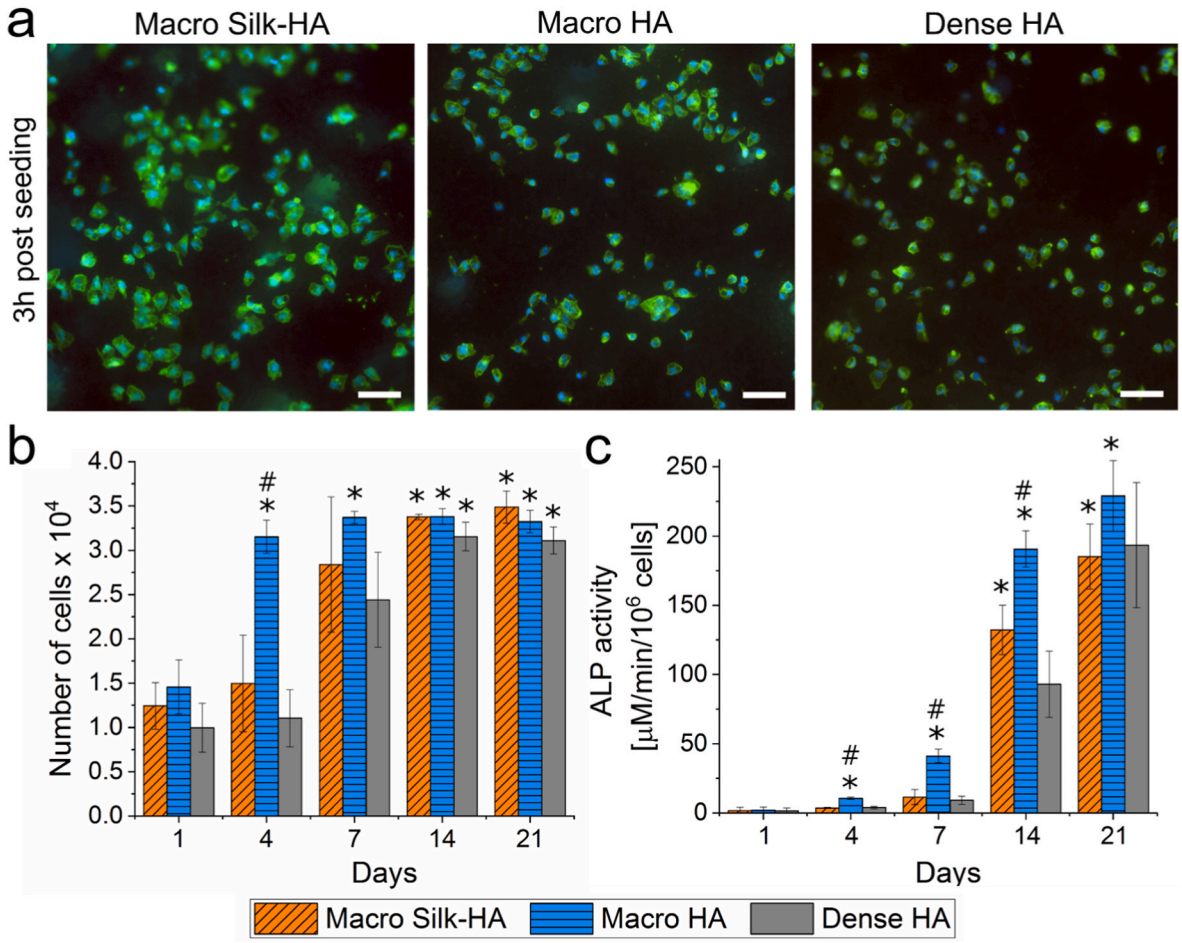

Fig. 6. Biological characterization of the HA-scaffolds. Top view of the scaffolds showing cell morphology and attachment of mMSCs stained with DAPI (blue) and phalloidin (green) at 3 h post seeding on Macro Silk-HA (left), Macro HA (middle) and Dense HA (right panel) (a). Scale bar 100 µm. Number of viable cells detected with LDH activity assay (b), and ALP activity as a measure of osteogenic differentiation of mMSCs at indicated time points during 3 weeks culture in Macro Silk-HA, Macro HA and Dense HA scaffolds (c). Statistically significant differences over time (compared to day 1) are indicted by an asterisk (*) at the designated time point. Differences between materials at a given time point are instead indicated by a hash (#). p-values < 0.05 were considered statistically significant. (For interpretation of the references to colour in this figure legend, the reader is referred to the Web version of this article.)

begun to increase for all scaffold types (Fig. 6c). This shows that the cells had started to differentiate into osteoblasts after an initial growth period. A significantly higher level of ALP activity was observed for Macro HA between 4 and 14 days compared to the other two scaffold types ($p < 0.005$ at day 4 and day 7, and $p < 0.05$ at day 14). However, the ALP-activity increased continuously for all samples during the entire culture period, and at day 21, no significant differences were observed between the groups, indicating that all of them supported osteogenic differentiation of mMSCs.

3.3.4. Cell migration behavior

Migration of mMSCs into the scaffolds was assessed by determining their infiltration distance from the scaffold surface to the interior at selected time points (Fig. 7). This analysis showed that the migration behavior was markedly different between the three scaffold variants (Fig. 7a). Notably, the cells seeded on the Macro HA had a starting position about three times more distant from the surface than cells on the Macro Silk-HA, but the infiltration distance barely doubled during the 3 weeks period. In contrast, the Macro Silk-HA showed a consistently increasing infiltration distance during the entire culture period (Fig. 7a). At the end point (day 21), the cells had migrated significantly further into the Macro Silk-HA scaffolds than into the two other scaffold types ($p < 0.01$). Moreover, when comparing the infiltration distance at day 21 with the position at 3 h, there was a significant difference for Macro Silk-HA ($p < 0.05$), neither found for Macro HA nor for Dense HA (Fig. 7a). Finally, when calculating the total migration over 3 weeks (mean infiltration distance at 3 h withdrawn from the mean infiltration distance at day 21), this was significantly higher for Macro Silk-HA compared to the other two scaffolds types (Fig. 7b, $p < 0.05$). Micrographs from day 21 showing cross sections of the scaffolds with cells at marked infiltration distances confirm this difference in migration behavior (Fig. 7c).

3.3.5. Cell-material interactions

The interaction between the cells and the materials was closely investigated by SEM analyses. Top view SEM micrographs confirmed a close interaction between the mMSCs and the microstructure of the HA scaffolds, with elongated protrusions from the mMSCs toward the crystals of the material surface, structures typical for established attachment or migration of cells (Fig. 8 and A6). Fluorescence micrographs indicate that cells grown on silk scaffolds exhibited a longer and more stretched out morphology than cells grown on the other scaffold formats at 1 and 3 weeks after seeding (Fig. A6).

4. Discussion

The use of composite scaffolds has been widely studied, where the mineral phase provides strength and the organic protein phase increases the materials' cytocompatibility [54]. However, to provide an environment that stimulates cell infiltration, a combination of adequate porosity and physico-chemical properties is required [11].

In this work, macroporous biomimetic hydroxyapatite (HA) was developed by foaming a cement paste using two different foaming agents – a recombinant functionalized silk protein (FN-silk) and a synthetic surfactant (polysorbate 80). A silk protein concentration of 2 mg/mL foamed for a short time maximized the total porosity of the resulting

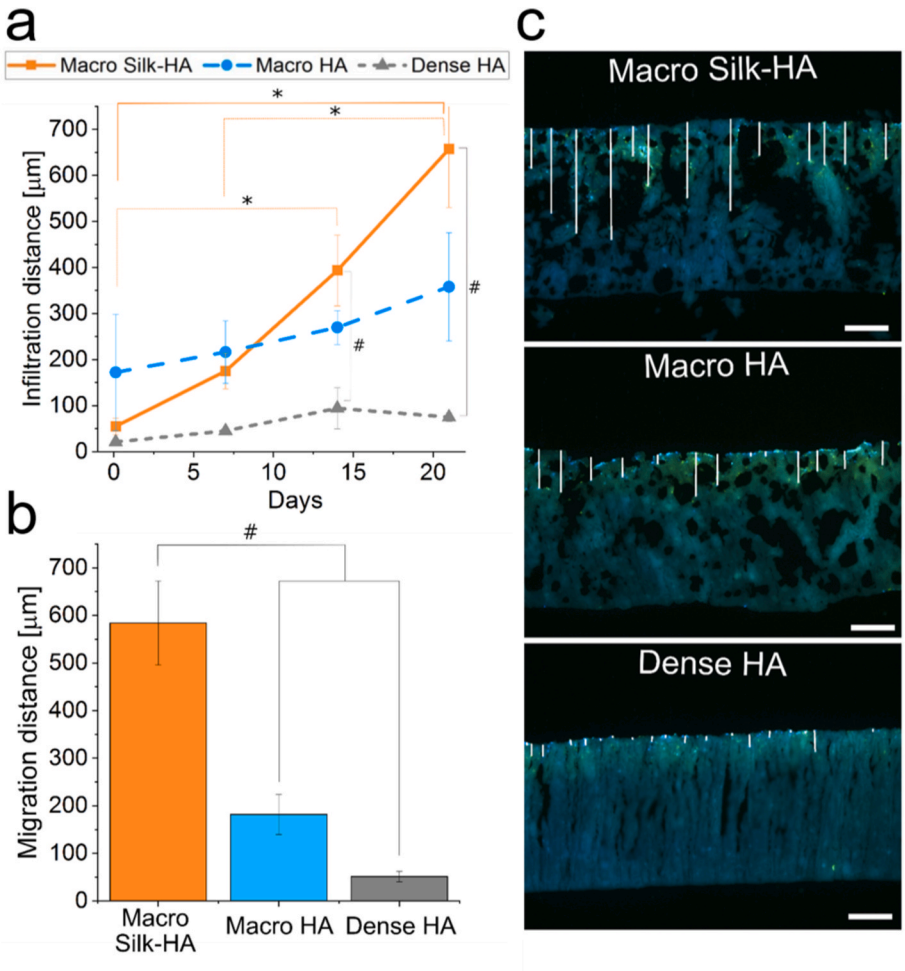

Fig. 7. Migration of mMSCs into HA scaffolds during 3 weeks culture. Cell infiltration relative to the top surface in µm for Macro Silk-HA, Macro HA and Dense HA (a). Migration distance, calculated by subtracting the mean starting position (at 3 h) from then mean final position (b). Fluorescence micrographs of cross-sections of Macro Silk-HA, Macro HA and Dense HA at 21 days where cells were stained with DAPI (blue) and phalloidin (green) showing the infiltration distance (white lines) from the top surface (c). Statistically significant differences over time are indicted by an asterisk (*). Differences between materials at a given time point are instead indicated by a hash (#) p-values <0.05 or less were considered statistically significant. Scale bars 100 µm. (For interpretation of the references to colour in this figure legend, the reader is referred to the Web version of this article.)

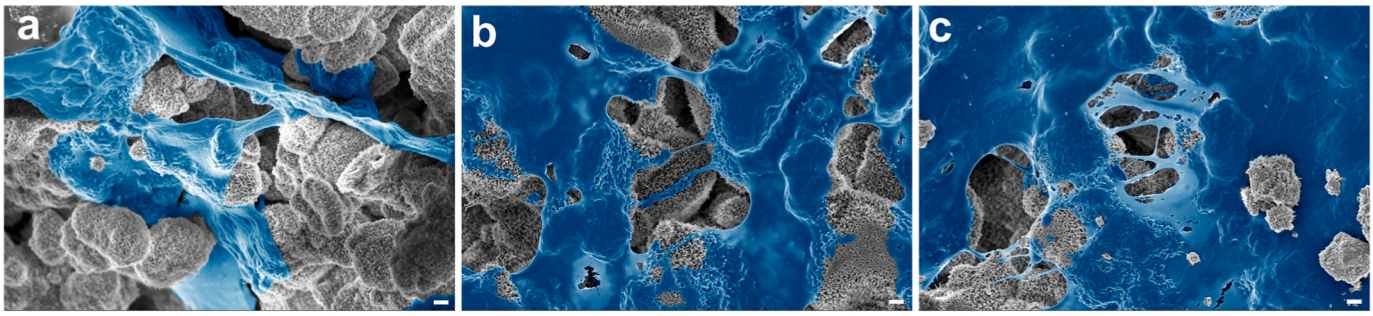

Fig. 8. SEM images showing mMSCs (blue) attaching to the surface of the Macro Silk-HA scaffolds at 3 h (a), 7 days (b), and 21 days (c) after seeding. Scale bar 1 μm. (For interpretation of the references to colour in this figure legend, the reader is referred to the Web version of this article.)

Macro Silk HA material (Fig. A3a). Silk protein assembles into solid silk structures when subjected to shear forces. However, a prolonged whipping after silk structures have formed would only cause the solid structures to be torn apart, causing aggregation and collapse of the foam. To mildly flatten the paste, without the use of a spatula, was also important to avoid disrupting the entrapped bubbles and therefore maintain the macroporosity (Fig. A3b).

Interestingly, the total porosity of Macro HA samples barely increased when augmenting the concentration of PS80. The porosity of Macro HA prepared with 0.25% PS80 was only 9.8 ± 5.0% whereas Macro Silk-HA resulted in samples with triple the amount of total porosity. To reach similar levels of total porosity in the two macroporous samples, the influence of NaP was investigated. While the total porosity of Macro Silk-HA experienced an increase of less than 10% by the addition of NaP, the corresponding increment was approximately 7-fold for the samples prepared with 0.10 and 0.25% PS80 (Fig. 2). These marked differences can probably be explained by the higher stability of the silk foam compared to PS foam (Fig. A2). A stable foam has a better ability to maintain the macroporous bubbles created in the cement foam while transforming into HA. In contrast, a foam with lower stability, as that obtained with PS80 foam, requires a faster cement setting process to be able to retain the macroporous template along its transformation into a solid material, which was achieved by adding NaP to the powder phase of the cement.

The SEM-micrographs of Macro Silk-HA and Macro HA confirmed that the samples containing NaP resulted in scaffolds with higher porosity. The addition of NaP was particularly effective in creating an open superficial porosity, which was associated to the intrinsic quicker setting on the surface due to the additional evaporation effect, therefore particularly potentiating the entrapment of pores within the matrix (Fig. 3). The effect of NaP was more pronounced for the Macro HA than for Macro Silk-HA, which again could be related to the stronger stability of the silk foam (Fig. A2), thus being independent of a faster setting to hold the porosity within the structure.

NaP has been widely used as an accelerant to enhance the setting reaction of apatite cements [55,56]. The acceleration in the setting reaction is due to the common-ion effect, which is caused by the addition of a weak electrolyte (*i.e.* NaP) that has one ion in common with the original compound (*i.e.* α-TCP) [55]. This leads to a decrease in solubility, causing a faster precipitation to reach the solubility equilibrium. Moreover, the faster setting reaction causing an increased total porosity in Macro HA could also be associated with the increase of pH of the liquid phase (2.5 wt% NaP in water leads to a pH of 9 [56]), which decreases the solubility of the calcium phosphate products [57].

The porosity features of these materials are complex, since macroporosity introduced by foaming agents was superimposed to the intrinsic microstructure found in biomimetic HA materials. For this reason, the materials were characterized using two complementary techniques: μ-CT and MIP. μ-CT provided information on both the open and closed porosity of the samples, since it determines the quantity of volume occupied by pores. However, it has to be taken into account that the resolution of this technique is limited, and only pores larger than 6.79 μm are detected, and therefore the submicrometric pores are overlooked. MIP was used to monitor the open or interconnected porosity in the range between 6 nm and 360 μm, by quantifying the pore entrance size diameter (PESD). Thus, rather than pore size this method determines the pore interconnection size, and large cavities connected by smaller necks are registered as porosity having the diameter of the necks (bottle-neck effect). For this reason, MIP provides information of the real accessibility of the pore network by cells as well as the diffusion of nutrients and oxygen [58].

To interpret the MIP results (Fig. 4a), it is necessary to recall that the HA obtained through a cementation reaction exhibits a highly porous structure due to the entangled network of crystals formed during the dissolution-precipitation process. Specifically, the intercrystal's porosity (<0.6 μm) is due to the voids present between the crystals, while the interaggregates's porosity (0.6–4 μm) is caused by the separation between the crystal aggregates nucleated surrounding the original α-TCP particles. The range of both intercrystals' and interaggregates porosity was larger for the dense HA because this material has a larger volume of dense structure, where these porosities are located (Fig. 4a). With regard to the macroporous HA samples, the extrinsically added porosity was found above 4 μm, thus offering pore openings large enough to allow cell migration into a scaffold [8–11]. Although the porosity measured by μ-CT, which corresponds to the extrinsic microporosity introduced by the foaming process, was similar between the two macroporous HA samples (Fig. 2), the results obtained by MIP revealed that the degree of interconnectivity of the macropores was larger for the Macro HA than for the Macro Silk-HA. The smaller macropore entrance sizes of the Macro Silk-HA can be associated to the higher stability of the silk foam. In contrast, the lower stability of the PS80 foam could have caused the coalescence of some bubbles, fusing them together and creating bigger windows between pores of around 50 μm within the Macro HA structure (Fig. 4). This correlates well with the bigger size of the windows observed in the extrinsic porosity of Macro HA in comparison to Macro Silk-HA, as also confirmed by the surface and cross-section images obtained by SEM (Fig. 5). Another parameter that could contribute to the smaller size of the pore interconnections of Macro Silk-HA revealed by the MIP analysis could be the masking effect of silk on the pore entrances of these samples (due to bottle-neck effect mentioned above) (Fig. 4), since thin FN-silk sheets partly covered some of the extrinsically generated pore entrances (Fig. 5 insets, white arrows).

Interestingly, the concordance between μ-CT (Fig. 2) and MIP analyses (Fig. 4b, extrinsic porosity) was lower than in other studies [30]. This could be explained by a reduced interconnectivity of the macropores, causing that MIP would allocate the volume of macropores to a smaller pore entrance size if the pores interconnections were not big enough. Since this effect was more clear for Macro Silk-HA (μ-CT: 38.0% *vs.* MIP: 11.8%) than for Macro HA (μ-CT: 35.0% *vs.* MIP: 24.3%), it could be hypothesized that the pore openings are narrowed by the presence of silk.

Despite the differences in crystal morphology, pore size and pore

entrance size distribution, the three scaffold types were chemically similar after 10 days of setting. The crystalline phases of the final scaffolds corresponded to low crystalline CDHA, with small traces of unreacted α-TCP accounting for less than 7% according to Rietveld refinement analysis (Fig. A4 and Table A2).

MSCs were cultured on the surface of the HA scaffolds to evaluate their adhesion, proliferation, differentiation and migration into the scaffolds. The enhanced spreading of MSCs on the Macro-Silk HA (Fig. 6a) could be related to the presence of the fibronectin-derived cell binding motif RGD previously shown to stimulate adhesion, proliferation, survival and migration of cells [36]. The ability to enable a fast adhesion is crucial *in vivo*, where recruited cells need to establish within the newly introduced material as soon as possible to increase its biocompatibility. MSCs are programmed to proliferate and migrate until a shift in the machinery occurs, initiating the cell differentiation towards the osteoblast phenotype [59]. This means that there is an opposite relationship between cell division and migration on one side, and differentiation on the other. Such a relationship was also reflected in the current study. The cellular metabolism evaluated using a LDH assay showed that the activity levels flattened out simultaneously with the onset of ALP activity (Fig. 6b and c).

The MSCs showed a slightly different behavior on the two macroporous HA scaffolds in terms of proliferation, migration and ALP activity. Macro HA yielded higher proliferation at early time points (Fig. 6b), which could explain the higher ALP values from these samples (Fig. 6c). The higher cellular confluence at the surface could create an environment where the MSCs were pushed into the osteogenic linage [60], as herein observed at an earlier stage for the Macro HA, compared to Silk Macro-HA. Noteworthy, both proliferation and ALP activity (Fig. 6b and c) reached similarly high levels in both Macro-Silk HA and Macro HA at the end stage of the culture. Importantly, cell migration on Macro-Silk HA greatly increased after 7 days (Fig. 7a), contributing to the increase in cell proliferation observed after 7 days. The ability of FN-silk to support osteogenic differentiation of MSCs when integrated in silk fibers was previously shown by alizarin Red staining [37]. Similarly, previous approaches incorporating RGD-motifs sequences have shown to increase the expression of osteogenic related genes [41], support enhanced mineralization [42] and new bone formation *in vivo* [44] even in the absence of macroporosity. In the current study, the combination of silk with an osteoconductive material such as HA most likely masked any enhancing osteogenic properties of the FN-silk protein.

Cell migration, which plays a critical role in scaffold-based bone engineering, is known to be governed by biochemical stimuli and cellular interactions, and is thus dependent on both substrate chemistry, topography and presence of binding sites for cells. As observed in the cross sections of the macroporous scaffolds (Fig. 5d and e), the surface-exposed pores were larger in the Macro HA than in the Macro Silk-HA, probably resulting in cells entering into the scaffold just by sedimentation. These differences in surface structure resulted in a somewhat deeper starting position for the cells on the Macro HA (*i.e.* mean 200 μm at 3 h after seeding), compared to Silk Macro-HA (mean 50 μm) (Fig. 7a). The presence of FN-silk along the walls of the pores (Fig. 5 insets, white arrows) probably contributed to an active movement of cells entering the pore network of the Macro Silk HA scaffolds, which was herein visualized as an increased infiltration of cells. This could explain why, already at day 7, cells were found at similar depths, and at the endpoint (day 21) cells had migrated much deeper in Macro-silk HA than in Macro HA (Fig. 7), indicating a faster migratory pace due to the silk present inside the scaffold (Fig. 5 insets, white arrows). This effect is even more remarkable if we take into account that the interconnectivity as determined by MIP was smaller for the Macro-silk HA than for the Macro HA scaffolds.

CPCs have been widely studied in the research community [61] and new formulations and applications are constantly being evaluated [62,63]. From a material properties perspective, the focus lies on overcoming some of the current CPCs shortcomings, such as the low degradation [64,65], poor injectability [30,66,67], and poor mechanical performance [65]. The development of macroporous HA loaded with silk is timely, since the porous structure will improve the degradation rate of the material [30] and at the same time promote cell migration, colonization and vascularization [30,37]. Moreover, the material has potential to be injected [24] and the silk's mechanical properties [68,69] could have a reinforcing effect on the ceramic scaffold.

5. Conclusion

Tissue engineering has the potential to regenerate bone with the support of synthetic scaffolds, which with a multiscale porosity can promote both protein adhesion and cell migration. In the current study we developed two types of macroporous HA by foaming the cement's liquid phase using either a recombinant FN-silk protein (Silk Macro-HA) or polysorbate 80 (Macro HA). The materials, which had macropores superimposed to the intrinsic microporosity of HA, yielded similar total porosity if a cement setting accelerant ($Na_2HPO_4{\cdot}2H_2O$, NaP) was added, which was especially important for Macro HA due to the lower stability of the polysorbate foam compared to the silk one. Although the resulting pore size entrances were larger for Macro HA than for Silk Macro-HA, MSCs had an enhanced cell migration towards the interior of the Silk Macro-HA scaffolds, likely due to the presence of cell binding motifs. Proliferation and differentiation of MSCs were less predominant on Silk Macro-HA at earlier stages but showed similar levels after two weeks of culture. The macroporosity of the Silk Macro-HA is expected to further enhance degradation and potential vascularization *in vivo*, although this remains to be evaluated in future studies.

Declaration of competing interest

The authors declare the following financial interests/personal relationships which may be considered as potential competing interests: M. Widhe, A. Diez-Escudero, Y. Liu, N. Ringström, M.P. Ginebra, C. Persson, G. Mestres declare that they have no conflicts of interest. M. Hedhammar has shares in Spiber Technologies AB, a company that aims to commercialize recombinant spider silk.

Acknowledgements

This work was supported by the Spanish Government (PID2019-103892RB-I00/AEI/10.13039/501100011033), the Generalitat de Catalunya (ICREA Academia Award), the Göran Gustafsson's Foundation (2017-1729 and 2021-2126), the Swedish Research Council Vetenskapsrådet (2017-05051), the Research Council for Sustainable Development FORMAS (2016-00781) and the Swedish Fund for Research Without Animal Experiments. The authors would like to express our gratitude towards Alejandro López for assistance in the Rietveld analysis, Meritxell Molmeneu for performing mercury intrusion porosimetry measurements and Victorine Lançon for her contribution in the initial cell culture studies.

Appendix A. Supplementary data

Supplementary data to this article can be found online at https://doi.org/10.1016/j.ceramint.2022.07.056.

References

[1] S. Bose, M. Roy, A. Bandyopadhyay, Recent advances in bone tissue engineering scaffolds, Trends Biotechnol. 30 (2012) 546–554, https://doi.org/10.1016/j.tibtech.2012.07.005.

[2] W. Wang, K.W.K. Yeung, Bone grafts and biomaterials substitutes for bone defect repair: a review, Bioact. Mater. 2 (2017) 224–247, https://doi.org/10.1016/j.bioactmat.2017.05.007.

[3] X. Pei, L. Ma, B. Zhang, J. Sun, Y. Sun, Y. Fan, Z. Gou, C. Zhou, X. Zhang, Creating hierarchical porosity hydroxyapatite scaffolds with osteoinduction by three-

dimensional printing and microwave sintering, Biofabrication 9 (2017), https://doi.org/10.1088/1758-5090/aa90ed, 045008.
[4] O. Gauthier, E. Goyenvalle, J.M. Bouler, J. Guicheux, P. Pilet, P. Weiss, G. Daculsi, Macroporous biphasic calcium phosphate ceramics versus injectable bone substitute: a comparative study 3 and 8 weeks after implantation in rabbit bone, J. Mater. Sci. Mater. Med. 12 (2001) 385–390, https://doi.org/10.1023/A:1011284517429.
[5] M. Bohner, F. Baumgart, Theoretical model to determine the effects of geometrical factors on the resorption of calcium phosphate bone substitutes, Biomaterials 25 (2004) 3569–3582, https://doi.org/10.1016/j.biomaterials.2003.10.032.
[6] A. Oryan, S. Alidadi, A. Moshiri, N. Maffulli, Bone regenerative medicine: classic options, novel strategies, and future directions, J. Orthop. Surg. Res. 9 (2014) 1–27, https://doi.org/10.1186/1749-799X-9-18.
[7] A. Diez-Escudero, M. Espanol, S. Beats, M.P. Ginebra, In vitro degradation of calcium phosphates: effect of multiscale porosity, textural properties and composition, Acta Biomater. 60 (2017) 81–92, https://doi.org/10.1016/j.actbio.2017.07.033.
[8] S.J. Hollister, Porous scaffold design for tissue engineering, Nat. Mater. 4 (2005) 518–524, https://doi.org/10.1038/nmat1421.
[9] P. Habibovic, H. Yuan, C.M. van der Valk, G. Meijer, C. a van Blitterswijk, K. de Groot, 3D microenvironment as essential element for osteoinduction by biomaterials, Biomaterials 26 (2005) 3565–3575, https://doi.org/10.1016/j.biomaterials.2004.09.056.
[10] C.M. Murphy, M.G. Haugh, F.J. O'Brien, The effect of mean pore size on cell attachment, proliferation and migration in collagen-glycosaminoglycan scaffolds for bone tissue engineering, Biomaterials 31 (2010) 461–466, https://doi.org/10.1016/j.biomaterials.2009.09.063.
[11] R.A. Perez, G. Mestres, Role of pore size and morphology in musculo-skeletal tissue regeneration, Mater. Sci. Eng. C. 61 (2016) 922–939, https://doi.org/10.1016/j.msec.2015.12.087.
[12] L. Guan, J.E. Davies, Preparation and characterization of a highly macroporous biodegradable composite tissue engineering scaffold, J. Biomed. Mater. Res., Part A 71 (2004) 480–487, https://doi.org/10.1002/jbm.a.30173.
[13] M.P. Ginebra, M. Espanol, Y. Maazouz, V. Bergez, D. Pastorino, Bioceramics and bone healing, EFORT Open Rev 3 (2018) 173–183, https://doi.org/10.1302/2058-5241.3.170056.
[14] F.C.M. Driessens, M.G. Boltong, O. Bermudez, J.A. Planell, Formulation and setting times of some calcium orthophosphate cements: a pilot study, J. Mater. Sci. Mater. Med. 4 (1993) 503–508, https://doi.org/10.1007/BF00120130.
[15] R.Z. LeGeros, Calcium phosphate-based osteoinductive materials, Chem. Rev. 108 (2008) 4742–4753, https://doi.org/10.1021/cr800427g.
[16] M. Espanol, R.A. Perez, E.B. Montufar, C. Marichal, A. Sacco, M.P. Ginebra, Intrinsic porosity of calcium phosphate cements and its significance for drug delivery and tissue engineering applications, Acta Biomater. (2009), https://doi.org/10.1016/j.actbio.2009.03.011.
[17] T.M.G. Chu, J.W. Halloran, S.J. Hollister, S.E. Feinberg, Hydroxyapatite implants with designed internal architecture, J. Mater. Sci. Mater. Med. 12 (2001) 471–478, https://doi.org/10.1023/A:1011203226053.
[18] Y.S. Dong, B. Liu, P.H. Lin, Q.G. Zhang, Y.P. Pu, Macroporous hydroxyapatite scaffold fabricated by foam impregnation, in: Key Eng. Mater., Trans Tech Publications Ltd, 2005, pp. 565–568, https://doi.org/10.4028/0-87849-967-9.565.
[19] H.H.K. Xu, E.F. Burguera, L.E. Carey, Strong, macroporous, and in situ-setting calcium phosphate cement-layered structures, Biomaterials 28 (2007) 3786–3796, https://doi.org/10.1016/j.biomaterials.2007.05.015.
[20] J.E. Barralet, L. Grover, T. Gaunt, A.J. Wright, I.R. Gibson, Preparation of macroporous calcium phosphate cement tissue engineering scaffold, Biomaterials 23 (2002) 3063–3072, https://doi.org/10.1016/S0142-9612(01)00401-X.
[21] W.J.E.M. Habraken, J.G.C. Wolke, A.G. Mikos, J.A. Jansen, PLGA microsphere/calcium phosphate cement composites for tissue engineering: in vitro release and degradation characteristics, J. Biomater. Sci. Polym. Ed. 19 (2008) 1171–1188, https://doi.org/10.1163/156856208785540136.
[22] P. Sepulveda, A.H. Bressiani, J.C. Bressiani, L. Meseguer, In Vivo Evaluation of Hydroxyapatite Foams, vol. 5, 2002, pp. 253–256.
[23] A. Almirall, G. Larrecq, J. Delgado, Fabrication of low temperature macroporous hydroxyapatite scaffolds by foaming and hydrolysis of an α-TCP paste, Biomaterials 25 (2004) 3671–3680, https://doi.org/10.1016/j.biomaterials.2003.10.066.
[24] M.-P. Ginebra, J.-A. Delgado, I. Harr, A. Almirall, S. Del Valle, J.A. Planell, Factors affecting the structure and properties of an injectable self-setting calcium phosphate foam, J. Biomed. Mater. Res., Part A 80A (2007) 351–361, https://doi.org/10.1002/jbm.a.30886.
[25] E.B. Montufar, T. Traykova, C. Gil, I. Harr, A. Almirall, A. Aguirre, E. Engel, J. A. Planell, M.P. Ginebra, Foamed surfactant solution as a template for self-setting injectable hydroxyapatite scaffolds for bone regeneration, Acta Biomater. 6 (2010) 876–885, https://doi.org/10.1016/j.actbio.2009.10.018.
[26] X. Huang, X. Miao, Novel porous hydroxyapatite prepared by combining H2O2 foaming with PU sponge and modified with PLGA and bioactive glass, J. Biomater. Appl. 21 (2007) 351–374, https://doi.org/10.1177/0885328206063905.
[27] A. Woesz, M. Rumpler, J. Stampfl, F. Varga, N. Fratzl-Zelman, P. Roschger, K. Klaushofer, P. Fratzl, Towards bone replacement materials from calcium phosphates via rapid prototyping and ceramic gelcasting, Mater. Sci. Eng. C (2005) 181–186, https://doi.org/10.1016/j.msec.2005.01.014.
[28] U. Gbureck, E. Vorndran, F.A. Müller, J.E. Barralet, Low temperature direct 3D printed bioceramics and biocomposites as drug release matrices, J. Contr. Release 122 (2007) 173–180, https://doi.org/10.1016/j.jconrel.2007.06.022.
[29] L. Jongpaiboonkit, J.W. Halloran, S.J. Hollister, Internal Structure Evaluation of Three-Dimensional Calcium Phosphate, vol. 3181, 2006, pp. 3176–3181, https://doi.org/10.1111/j.1551-2916.2006.01143.x.
[30] A. Barba, Y. Maazouz, A. Diez-Escudero, K. Rappe, M. Espanol, E.B. Montufar, C. Öhman-Mägi, C. Persson, P. Fontecha, M.-C. Manzanares, J. Franch, M.-P. Ginebra, Osteogenesis by foamed and 3D-printed nanostructured calcium phosphate scaffolds: effect of pore architecture, Acta Biomater. 79 (2018) 135–147, https://doi.org/10.1016/j.actbio.2018.09.003.
[31] S.L. McNamara, J. Rnjak-Kovacina, D.F. Schmidt, T.J. Lo, D.L. Kaplan, Silk as a biocohesive sacrificial binder in the fabrication of hydroxyapatite load bearing scaffolds, Biomaterials 35 (2014) 6941–6953, https://doi.org/10.1016/j.biomaterials.2014.05.013.
[32] M. Saleem, S. Rasheed, C. Yougen, Silk fibroin/hydroxyapatite scaffold: a highly compatible material for bone regeneration, Sci. Technol. Adv. Mater. 21 (2020) 242–266, https://doi.org/10.1080/14686996.2020.1748520.
[33] M. Widhe, J. Johansson, M. Hedhammar, A. Rising, Current progress and limitations of spider silk for biomedical applications, Biopolymers 97 (2012) 468–478, https://doi.org/10.1002/bip.21715.
[34] M. Widhe, H. Bysell, S. Nystedt, I. Schenning, M. Malmsten, J. Johansson, A. Rising, M. Hedhammar, Recombinant spider silk as matrices for cell culture, Biomaterials 31 (2010) 9575–9585, https://doi.org/10.1016/J.BIOMATERIALS.2010.08.061.
[35] M. Widhe, U. Johansson, C.-O. Hillerdahl, M. Hedhammar, Recombinant spider silk with cell binding motifs for specific adherence of cells, Biomaterials 34 (2013) 8223–8234, https://doi.org/10.1016/J.BIOMATERIALS.2013.07.058.
[36] M. Widhe, N.D. Shalaly, M. Hedhammar, A fibronectin mimetic motif improves integrin mediated cell biding to recombinant spider silk matrices, Biomaterials 74 (2016) 256–266, https://doi.org/10.1016/J.BIOMATERIALS.2015.10.013.
[37] U. Johansson, M. Widhe, N.D. Shalaly, I.L. Arregui, L. Nilebäck, C.P. Tasiopoulos, C. Åstrand, P.O. Berggren, C. Gasser, M. Hedhammar, Assembly of functionalized silk together with cells to obtain proliferative 3D cultures integrated in a network of ECM-like microfibers, Sci. Rep. 9 (2019) 1–13, https://doi.org/10.1038/s41598-019-42541-y.
[38] C. Fredriksson, M. Hedhammar, R. Feinstein, K. Nordling, G. Kratz, J. Johansson, F. Huss, A. Rising, Tissue response to subcutaneously implanted recombinant spider silk: an in vivo study, Materials (Basel) 2 (2009) 1908–1922, https://doi.org/10.3390/ma2041908.
[39] M. Stark, S. Grip, A. Rising, M. Hedhammar, W. Engström, G. Hjälm, J. Johansson, Macroscopic fibers self-assembled from recombinant miniature spider silk proteins, Biomacromolecules 8 (2007) 1695–1701, https://doi.org/10.1021/bm070049y.
[40] W. Theinhan, J. Liu, M. Tang, W. Chen, L. Cheng, H.H.K. Xu, Induced pluripotent stem cell-derived mesenchymal stem cell seeding on biofunctionalized calcium phosphate cements, Bone Res 1 (2013) 371–384, https://doi.org/10.4248/BR201304008.
[41] W. Chen, W. Thein-Han, M.D. Weir, Q. Chen, H.H.K. Xu, Prevascularization of biofunctional calcium phosphate cement for dental and craniofacial repairs, Dent. Mater. 30 (2014) 535–544, https://doi.org/10.1016/J.DENTAL.2014.02.007.
[42] W. Thein-Han, J. Liu, H.H.K. Xu, Calcium phosphate cement with biofunctional agents and stem cell seeding for dental and craniofacial bone repair, Dent. Mater. 28 (2012) 1059–1070, https://doi.org/10.1016/J.DENTAL.2012.06.009.
[43] H. Zhou, W. Chen, M.D. Weir, H.H.K. Xu, Biofunctionalized calcium phosphate cement to enhance the attachment and osteodifferentiation of stem cells released from fast-degradable alginate-fibrin microbeads, Tissue Eng. 18 (2012) 1583–1595, https://doi.org/10.1089/TEN.TEA.2011.0604/ASSET/IMAGES/LARGE/FIGURE7.JPEG.
[44] W. Schneiders, A. Reinstorf, W. Pompe, R. Grass, A. Biewener, M. Holch, H. Zwipp, S. Rammelt, Effect of modification of hydroxyapatite/collagen composites with sodium citrate, phosphoserine, phosphoserine/RGD-peptide and calcium carbonate on bone remodelling, Bone 40 (2007) 1048–1059, https://doi.org/10.1016/J.BONE.2006.11.019.
[45] M. Hedhammar, H. Bramfeldt, T. Baris, M. Widhe, G. Askarieh, K. Nordling, S. Von Aulock, J. Johansson, Sterilized recombinant spider silk fibers of low pyrogenicity, Biomacromolecules 11 (2010) 953–959, https://doi.org/10.1021/bm9014039.
[46] N. Doebelin, R. Kleeberg, Profex: a graphical user interface for the Rietveld refinement program BGMN, J. Appl. Crystallogr. 48 (2015) 1573–1580, https://doi.org/10.1107/S1600576715014685.
[47] J. Bergmann, P. Friedel, R. Kleeberg, BGMN - a new fundamental parameters based Rietveld program for laboratory X-ray sources, it's use in quantitative analysis and structure investigations, IUCr Comm. Powder Diffr. Newsl. 20 (1998) 5–8, accessed June 21, 2022, https://www.scienceopen.com/document?vid=274b072e-c613-44f6-a8f2-c59bd2147547.
[48] T. Taut, R. Kleeberg, J. Bergmann, The new seifert Rietveld program BGMN and its application to quantitative phase analysis, Mater. Struct. 5 (1998) 57–66.
[49] A. Belkly, M. Helderman, V.L. Karen, P. Ulkch, New developments in the inorganic crystal structure Database (ICSD): accessibility in support of materials research and design, Acta Crystallogr. Sect. B Struct. Sci. 58 (2002) 364–369, https://doi.org/10.1107/S0108768102006948.
[50] J.-M. Sadowska, J. Guillem-Marti, E.B. Montufar, M. Espanol, M.-P. Ginebra, Biomimetic versus sintered calcium phosphates: the in vitro behavior of osteoblasts and mesenchymal stem cells, Tissue Eng. 23 (2017) 1297–1309, https://doi.org/10.1089/ten.tea.2016.0406.
[51] C. Vater, P. Kasten, M. Stiehler, Culture media for the differentiation of mesenchymal stromal cells, Acta Biomater. 7 (2011) 463–477, https://doi.org/10.1016/j.actbio.2010.07.037.

[52] H.C. Tenenbaum, Levamisole and inorganic pyrophosphate inhibit beta-glycerophosphate induced mineralization of bone formed in vitro, Bone Miner. 3 (1987) 13–26.
[53] H.J. Prins, A.K. Braat, D. Gawlitta, W.J.A. Dhert, D.A. Egan, E. Tijssen-Slump, H. Yuan, P.J. Coffer, H. Rozemuller, A.C. Martens, In vitro induction of alkaline phosphatase levels predicts in vivo bone forming capacity of human bone marrow stromal cells, Stem Cell Res. 12 (2014) 428–440, https://doi.org/10.1016/j.scr.2013.12.001.
[54] A.R. Armiento, L.P. Hatt, G.S. Rosenberg, K. Thompson, M.J. Stoddart, Functional biomaterials for bone regeneration: a lesson in complex biology, Adv. Funct. Mater. 30 (2020), 1909874, https://doi.org/10.1002/adfm.201909874.
[55] E. Fernández, M.G. Boltong, M.P. Ginebra, O. Bermúdez, F.C.M. Driessens, J. A. Planell, Common ion effect on some calcium phosphate cements, Clin. Mater. 16 (1994) 99–103, https://doi.org/10.1016/0267-6605(94)90103-1.
[56] E.B. Montufar, Y. Maazouz, M.P. Ginebra, Relevance of the setting reaction to the injectability of tricalcium phosphate pastes, Acta Biomater. 9 (2013) 6188–6198, https://doi.org/10.1016/j.actbio.2012.11.028.
[57] R.G. Carrodeguas, S. De Aza, α-Tricalcium phosphate: synthesis, properties and biomedical applications, Acta Biomater. 7 (2011) 3536–3546, https://doi.org/10.1016/j.actbio.2011.06.019.
[58] D. Pastorino, C. Canal, M.P. Ginebra, Multiple characterization study on porosity and pore structure of calcium phosphate cements, Acta Biomater. 28 (2015) 205–214, https://doi.org/10.1016/j.actbio.2015.09.017.
[59] E. Birmingham, G.L. Niebur, P.E. Mchugh, G. Shaw, F.P. Barry, L.M. McNamara, Osteogenic differentiation of mesenchymal stem cells is regulated by osteocyte and osteoblast cells in a simplified bone niche, Eur. Cell. Mater. 23 (2012) 13–27, https://doi.org/10.22203/eCM.v023a02.
[60] F.A.M. Abo-Aziza, A.A. Zaki, The impact of confluence on bone marrow mesenchymal stem (BMMSC) proliferation and osteogenic differentiation, Int. J. Hematol. Stem Cell Res. 11 (2017) 121–132.
[61] H.H.K. Xu, P. Wang, L. Wang, C. Bao, Q. Chen, M.D. Weir, L.C. Chow, L. Zhao, X. Zhou, M.A. Reynolds, Calcium phosphate cements for bone engineering and their biological properties, Bone Res 5 (2017) 1–19, https://doi.org/10.1038/boneres.2017.56.
[62] V.M. Bulsara, G.S. Kim, A.M. Fouad, M.K. Bulsara, P.L. Santa Maria, Middle cranial fossa approach to repair tegmen dehiscence using self-setting calcium phosphate cement: a retrospective case review, Otol. Neurotol. 42 (2021) 931–937, https://doi.org/10.1097/MAO.0000000000003110.
[63] F. Pourdanesh, N. Latifi, F. Latifi, Complications after craniofacial reconstruction with calcium phosphate cements: a case report and review of the literature, J. Korean Assoc. Oral Maxillofac. Surg. 44 (2018) 207–211, https://doi.org/10.5125/jkaoms.2018.44.5.207.
[64] I. Lodoso-Torrecilla, J.J.J.P. van den Beucken, J.A. Jansen, Calcium phosphate cements: optimization toward biodegradability, Acta Biomater. 119 (2021) 1–12, https://doi.org/10.1016/j.actbio.2020.10.013.
[65] L. Schröter, F. Kaiser, S. Stein, U. Gbureck, A. Ignatius, Biological and mechanical performance and degradation characteristics of calcium phosphate cements in large animals and humans, Acta Biomater. 117 (2020) 1–20, https://doi.org/10.1016/j.actbio.2020.09.031.
[66] R. O'Neill, H.O. McCarthy, E.B. Montufar, M.P. Ginebra, D.I. Wilson, A. Lennon, N. Dunne, Critical review: injectability of calcium phosphate pastes and cements, Acta Biomater. 50 (2017) 1–19, https://doi.org/10.1016/j.actbio.2016.11.019.
[67] A.M. Yousefi, A review of calcium phosphate cements and acrylic bone cements as injectable materials for bone repair and implant fixation, J. Appl. Biomater. Funct. Mater. 17 (2019), https://doi.org/10.1177/2280800019872594.
[68] B.B. Mandal, A. Grinberg, E.S. Gil, B. Panilaitis, D.L. Kaplan, High-strength silk protein scaffolds for bone repair, Proc. Natl. Acad. Sci. U. S. A. 109 (2012) 7699–7704, https://doi.org/10.1073/pnas.1119474109.
[69] Z. Dong, D. Wu, H. Engqvist, J. Luo, C. Persson, Silk fibroin hydrogels induced and reinforced by acidic calcium phosphate – a simple way of producing bioactive and drug-loadable composites for biomedical applications, Int. J. Biol. Macromol. 193 (2021) 433–440, https://doi.org/10.1016/j.ijbiomac.2021.10.160.